PAPER

Check for updates

Facile synthesis of magnetic intelligent sensors for the pH-sensitive controlled capture of Cr(VI)†

Peixin Hu,[a] Hechao Lu,[a] Qinting He,[a] Fang Ren,[a] Juan Wu � *[ab] and Wei Jiang[b]

In this work, intelligent pH-sensitive sensors (Fe_3O_4/RhB@PAM) for Cr(VI) detection were successfully synthesized based on polyacrylamide (PAM) and Rhodamine B (RhB) co-modified Fe_3O_4 nanocomposites. The characterization results indicated that the sensors had many favorable properties, including suitable size, stable crystal structure and excellent magnetic response performance (47.59 emu g^{-1}). In addition, the fluorescence changes during the detection process indicated that Fe_3O_4/RhB@PAM were "ON−OFF" intelligent sensors. When the Fe_3O_4/RhB@PAM sensors were placed in acidic Cr(VI) solution (pH 4), PAM acted as a pH-responsive "gatekeeper" releasing RhB, and the fluorescence intensity of released RhB was weakened by the complexation of Cr(VI). Furthermore, the fluorescence changes of the magnetic sensors were remarkably specific for Cr(VI) even in the presence of other competitive cations, and the limit of detection (LOD) for Cr(VI) was lower (0.347 μM) than the value recommended by the World Health Organization (0.96 μM). All the results presented in this study showed that the Fe_3O_4/RhB@PAM sensors had significant potential for Cr(VI) detection in acidic environmental samples.

1. Introduction

Among heavy metal pollutants, hexavalent chromium ions (Cr(VI)) have attracted much attention owing to their high toxicity and migration.[1] Cr(VI) in wastewater mainly comes from printing, dyeing, leather tanning, electroplating and metallurgy industries, among others.[2–4] Studies have shown that Cr(VI) can cause various problems to the human body, such as kidney and liver damage, gastrointestinal irritation and skin allergy.[5–7] The World Health Organization's International Agency for Research on Cancer (IARC) has classified Cr(VI) as a group 1 carcinogen.[8] Furthermore, the World Health Organization (WHO) also specifies the maximum acceptable levels of Cr(VI) in drinking water and industrial wastewater, which are 50 μg L^{-1} and 250 μg L^{-1}, respectively.[9,10] Therefore, there is an urgent need to establish efficient strategies for Cr(VI) detection in aqueous media.

Conventional methods for heavy-metal detection such as inductively coupled plasma atomic emission spectroscopy (ICP-AES), atomic adsorption spectroscopy (AAS), X-ray fluorescence (XRF), and inductively coupled plasma mass spectroscopy (ICP-MS) are highly sensitive, specific, and precise. However, most

techniques mentioned above are not suitable for the real-time on-site monitoring of heavy metal ions because of bulky instruments, high cost, and the requirement of trained personnel to operate them.[11,12] Thus, it is an urgent need to develop an intelligent, convenient, sensitive, selective, inexpensive, and non-polluting analytical method for Cr(VI) detection. In this regard, colorimetric sensors such as dyes,[13,14] polymers,[15,16] and nanomaterials[17,18] have been widely used for their excellent visualization, high selectivity and sensitivity. For the past few years, rhodamine B-based fluorescent dyes have been widely used for sensing because of the broad emission wavelength, high fluorescence quantum yield, and large extinction coefficient properties of rhodamine B.[19] D. Sahu *et al.*[20] developed a Ag/r-GO@RhB nanosensor for the detection of Hg^{2+} in aqueous media, with a low cost, high efficiency, and small detection limit of 2 nM at optimal pH and contact time. S. E. Hooshmand *et al.*[21] designed a novel naked-eye colorimetric probe based on rhodamine B for detecting nickel ions. When the probe met the target ions, the color changed from colorless to pink, and the detection limit was 0.3 μmol mL^{-1}. I. Y. Denisyuk *et al.*[22] prepared a polymer membrane fixed molecular form of rhodamine B for the detection of lead ions in water. The complexation of rhodamine B and lead led to changes in the adsorption and refraction parameters of the polymer composition, and the sensitivity was as high as 0.001 mg L^{-1}, which was below the maximum allowable concentration. However, there are still some shortcomings in these reported sensors, such as time-consuming operation, non-recyclability, and limited practical environmental applications. Moreover, there are few

[a]*Jiangsu Key Laboratory of E-waste Recycling, School of Resources and Environmental Engineering, Jiangsu University of Technology, Changzhou 213001, China. E-mail: jintanwujuan@163.com; Tel: +86-18906110982*

[b]*National Special Superfine Powder Engineering Research Center, Nanjing University of Science and Technology, Nanjing 210094, China*

sensors for rapid acid reaction detection of Cr(vi). Therefore, it is very important to develop a pH-sensitive, environment-friendly, highly selective and sensitive sensor that can respond quickly to Cr(vi) detection.

In recent years, the continuous development of nanoscience and technology has promoted the application of nanomaterials in the environmental field.[23–27] Magnetic nanoparticles, especially Fe_3O_4 nanoparticles, have attracted extensive attention due to their characteristics of superparamagnetism, ultra-fine size and low environmental impact,[28,29] and have been widely used in the fields of detection,[30,31] analysis,[32,33] environmental prevention[34] and control.[35,36] Considering these advantages, a simple, rapid, effective and pH-sensitive sensor (Fe_3O_4/RhB@PAM) was designed to capture Cr(vi) based on Rhodamine B (RhB), Fe_3O_4 nanoparticles and acrylamide (Fig. 1). Among them, Fe_3O_4 particles were used as magnetic response carriers to facilitate the recovery of the sensors, and a large number of amino groups in the polyacrylamide structural unit gave the sensor good hydrophilicity.[37] The Fe_3O_4 particles and RhB were embedded by PAM during the polymerization process. When

the Fe_3O_4/RhB@PAM sensor was added into acidic Cr(vi) aqueous solution, the change in the fluorescence signal was realized through the hydrolysis of PAM and the complexation of RhB with chromium Cr(vi) in Fe_3O_4/RhB@PAM sensors. Furthermore, the detected sensors could be enriched by an external magnetic field so as to avoid secondary pollution while providing an ideal solution for the intelligent and efficient capture of Cr(vi) in acidic solution.

2. Materials and methods

2.1. Materials

Ferric chloride ($FeCl_3 \cdot 6H_2O$), sodium acetate (NaAc) and ethylene glycol (EG) were supplied by Sinopharm Chemical Reagent Co., Ltd. 1-(3-Dimethylaminopropyl)-3-ethylcarbodiimide hydrochloride (EDC), polyethylene glycol dicarboxylic acid (PEG, $M_w = 600$), N-hydroxysuccinimide (NHS) and Rhodamine B (RhB) were purchased from Sigma-Aldrich. 1,6-Hexanediamine, sodium hexametaphosphate, acrylamide (AM) and potassium persulfate were purchased from Aladdin.
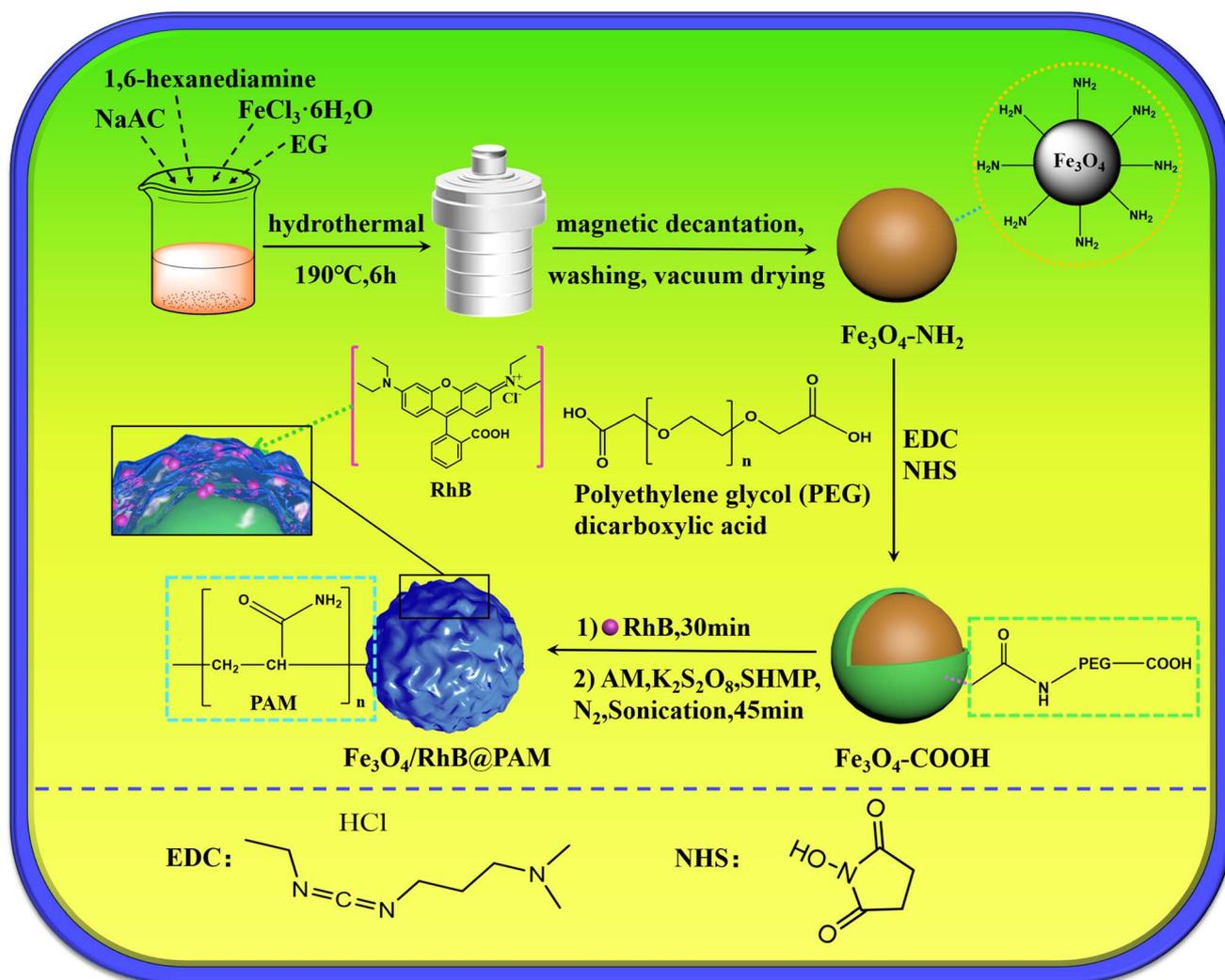

Fig. 1 Schematic illustration of the preparation process of Fe_3O_4/RhB@PAM sensors.

All chemicals were analytical grade and used without further purification. All other chemicals and solvents used in this study were of high analytical grade and commercially available.

2.2. Synthesis of Fe_3O_4–NH_2

Fe_3O_4–NH_2 nanoparticles were synthesized through a one-step hydrothermal method. Firstly, 5.0 g of 1,6-hexanediamine was added into 30 mL EG and completely dissolved at 50 °C in a water bath. Then, 1.0 g $FeCl_3 \cdot 6H_2O$ and 2.0 g NaAc were added and dissolved under sonication. Subsequently, the mixture was transferred to a 100 mL polytetrafluoroethylene-lined stainless-steel autoclave and reacted at 190 °C for 6 h. After the reaction was completed, the products were collected by a magnet and washed with ethanol and water three times. Finally, the Fe_3O_4–NH_2 nanoparticles were dried under vacuum at 35 °C.

2.3. Preparation of Fe_3O_4–COOH

100 mg EDC and 100 mg NHS were added into 10 mL PBS buffer solution (pH 7.2), then 5 mL PBS buffer solution containing PEG (5.13 M) was added, and the mixture was stirred at room temperature for 4 h. After that, 1.008 g Fe_3O_4–NH_2 nanoparticles were dispersed in 5 mL PBS buffer solution and added into the above reaction. Then, stirring and the reaction were continued for 24 h. Finally, the Fe_3O_4–COOH nanoparticles were collected by magnetic decantation and washed three times with water.

2.4. Preparation of Fe_3O_4/RhB@PAM nanosensors

Briefly, 0.075 g of the freshly prepared Fe_3O_4–COOH nanoparticles were dispersed in 150 mL ultra-pure water, then 1 mL RhB solution (0.2 mM) was slowly added. The mixture was stirred at room temperature for 30 min. After that, 1.422 g AM, 2.447 g of sodium hexametaphosphate and 0.108 g of potassium persulfate were added, and the mixture was sonicated and stirred vigorously for 45 min at 35 °C under N_2 atmosphere. Finally, the products were collected by a magnet and washed with ethanol and water three times. The Fe_3O_4/RhB@PAM nanosensors were dried under vacuum at 30 °C. The upper liquid from the separation and washing process was collected for UV-vis analysis to obtain the loading rate of RhB (87.5%).

2.5. Characterization

The size and morphology of the samples were characterized by high resolution transmission electron microscopy (HRTEM, Model Tecnai G2F30-Twin, FEI Co. Ltd, USA). The crystalline phases were recorded using X-ray diffraction (XRD, Bruker Co., Ltd, Germany) in the 2θ range of 10–80°. The surface chemical composition was characterized by X-ray photoelectron spectroscopy (XPS, Thermo Scientific Escalab 250). Fourier-transform infrared (FT-IR) spectra were recorded on a Vector 22 spectrometer (Bruker Co. Ltd, Germany) using the KBr pellet technique. The thermal stability of the dry samples was measured by thermogravimetric analysis (TGA, Model TA2100, TA Instruments, USA) under N_2 at a heating rate of 10 °C min^{-1} over the range of 50–700 °C. The magnetic properties of the synthesized materials were studied by a vibrating sample magnetometer (VSM, Model 7410, Lake Shore Co., Ltd, USA) at room temperature. The UV-vis absorbance spectra were recorded by UV-vis spectrophotometry (Nanjing Feile Instrument Co., Ltd). Fluorescence spectra were recorded by a fluorescence spectrophotometer (RF-6000, Shimadzu Co. Ltd, Japan).

3. Results and discussion

3.1. Characterization of the sample

The morphology of the Fe_3O_4/RhB@PAM nanosensors was characterized by HRTEM. As shown in Fig. 2a, Fe_3O_4/RhB@PAM has a core–shell structure similar to the outer transparent capsule ball, and the average particle size of Fe_3O_4/RhB@PAM is about 23.73 nm (Fig. 2b). Fig. 2c shows the electron diffraction pattern of Fe_3O_4/RhB@PAM, with six distinct diffraction rings corresponding to each crystal face of magnetite (Fe_3O_4) nanocrystals. Fig. 2d is a typical HRTEM image of Fe_3O_4/RhB@PAM with many lattice planes and good crystallinity. The measured plane spacing of all the lattice fringes is 0.29 nm, corresponding to the (220) lattice plane of face-centered cubic (fcc) Fe_3O_4.

To further confirm the successful preparation of the nanosensors, the elemental mapping of Fe, N, and O corresponding to Fe_3O_4/RhB@PAM nanosensors was carried out, as illustrated in Fig. 3. The uniform distribution of Fe, N, and O elements among the nanoparticles indicates that the Fe_3O_4 particles are homogeneously coated by PAM. Moreover, the peaks of O, Fe and N elements are presented in the energy dispersive spectra (EDS) (Fig. S1†), conforming the existence of RhB and PAM. It should be noted that the C and Cu elements are derived from the carbon film copper mesh used to support the samples during the HRTEM testing process.

The composition and crystallinity of Fe_3O_4–NH_2, Fe_3O_4–COOH and Fe_3O_4/RhB@PAM were investigated by XRD. As can be seen in Fig. 4, all the samples have six major reflections that appear in at about 30.1°, 35.4°, 43.0°, 53.3°, 57.1° and 62.5°, which can be indexed as the (220), (311), (400), (422), (511) and (440) diffraction peaks of the inverse spinel structure of Fe_3O_4 (JCPDS no. 19-0629), respectively, indicating that the polymerization coating process does not significantly result in the phase change of Fe_3O_4. In addition, Fe_3O_4/RhB@PAM has a broad characteristic peak at $2\theta = 21.5°$, which could be attributed to the diffraction peak of PAM.[38] All of these further confirm the successful synthesis of Fe_3O_4/RhB@PAM nanosensors.

The surface composition of the prepared Fe_3O_4/RhB@PAM was determined by XPS (Fig. 5).[39] As can be seen from Fig. 5a, the sensors contain Fe, O, C, N and Cl elements, where Fe comes from Fe_3O_4, C and N come from RhB and PAM, and Cl comes from RhB. Fig. 5b shows the characteristic peaks of Fe, whose binding energies appear at 710.8.0 eV and 724.9 eV, corresponding to Fe $2p_{3/2}$ and Fe $2p_{1/2}$, respectively.[40] A group of peaks with binding energy of 710.0 eV and 722.5 eV belong to Fe^{2+}, and a group of peaks with binding energy of 712.7 eV and 727.4 eV belong to Fe^{3+}, confirming the existence of Fe_3O_4. In Fig. 5c, the peaks at about 401.54 eV and 399.45 eV are attributable to the nitrogen of the amide groups in PAM and positively charged nitrogen in the quaternary ammonium salt of
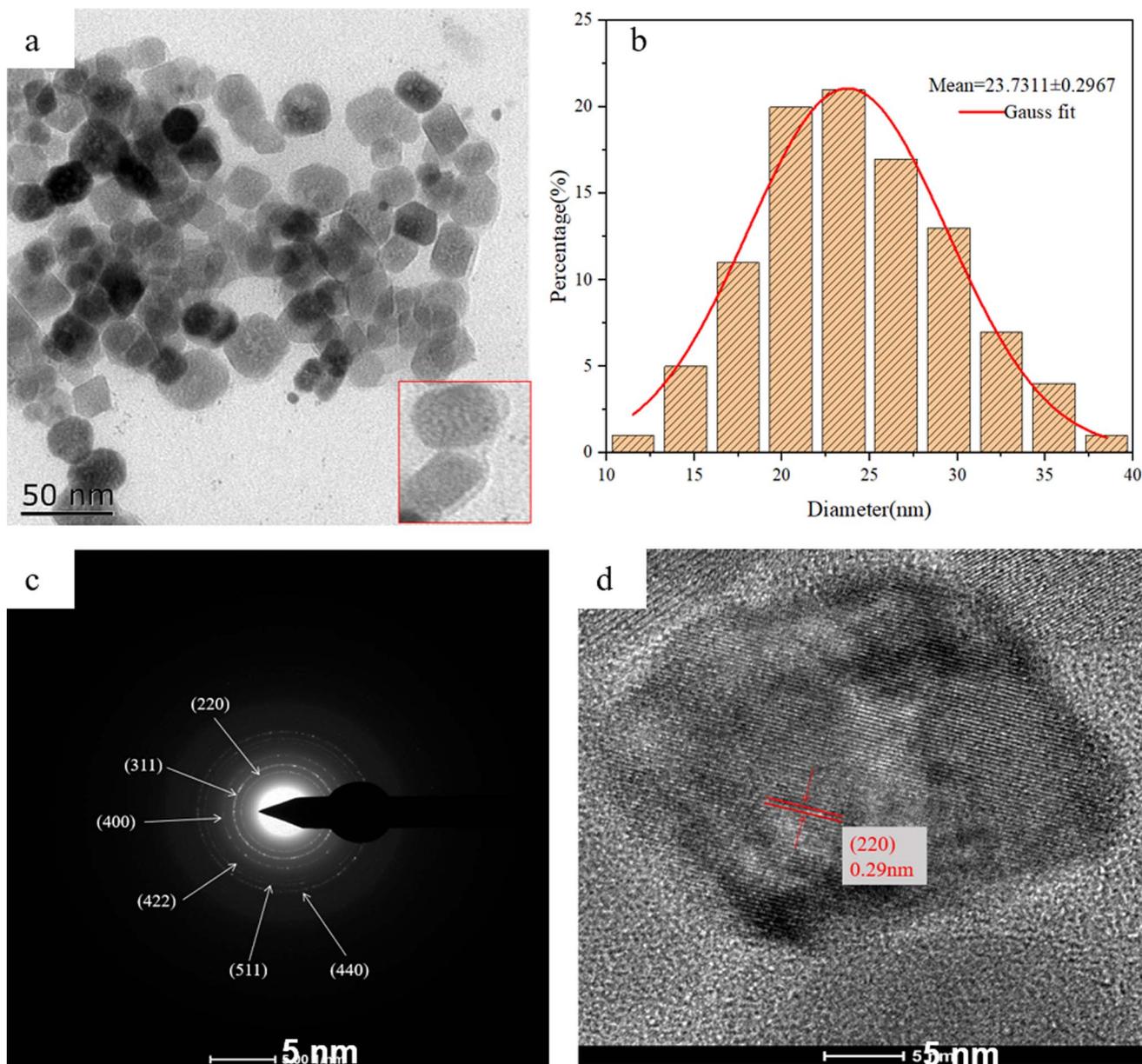
Fig. 2 HRTEM images of (a and d) Fe_3O_4/RhB@PAM nanosensors, (c) the electron diffraction pattern of Fe_3O_4/RhB@PAM nanosensors and (b) the size distribution of Fe_3O_4/RhB@PAM nanosensors.

RhB,[41] which indicates that Fe_3O_4/RhB is successfully coated by PAM. As shown in Fig. 5d, the C 1s XPS spectrum of Fe_3O_4/RhB@PAM shows three peaks at 284.8 eV, 286.2 eV and 288.6 eV, which are attributed to C–C, C–O and C=O bonds, respectively. The O 1s spectrum can be curve-fitted into three peaks with binding energies at about 529.4 eV, 531.2 eV and 533.1 eV (Fig. 5e); this may be caused by the –OH functional group and the low binding energy O^{2-} anion of Fe_3O_4/RhB@PAM. In addition, the characteristic peaks of Cl 2p appear at about 198.42 eV and 200.76 eV, further confirming the existence of RhB (Fig. 5f).[42] All the above results confirm the successful preparation of Fe_3O_4/RhB@PAM sensors.

The results of FT-IR spectroscopy are shown in Fig. S2;† the peaks at 581 cm^{-1} appearing in all the curves are attributed to the

typical Fe–O symmetric stretching vibration of Fe_3O_4.[43] For Fe_3O_4–NH_2 nanoparticles (Fig. S2a†), the peak at 3414 cm^{-1} might be attributed to the stretching vibration of N–H, and the signal at 1564 cm^{-1} is the deformation vibration absorption peak of N–H. The peaks at 2928 cm^{-1} and 2857 cm^{-1} are attributed to the symmetric and asymmetric stretching vibration of –CH_2, respectively, and the stretching vibration of C–N is at 1061 cm^{-1}. All of these results indicated that 1,6-hexanediamine was successfully grafted on the surface of Fe_3O_4.[44] However, after carboxylation, the characteristic peak of 1,6-hexanediamine disappeared. As shown in Fig. S2b,† the signal that appeared at 3436 cm^{-1} might be attributed to the stretching vibration of –OH, and the C=O characteristic absorption peak of amide is at 1688 cm^{-1}. The peaks at 1436 cm^{-1} and 1066 cm^{-1} correspond to
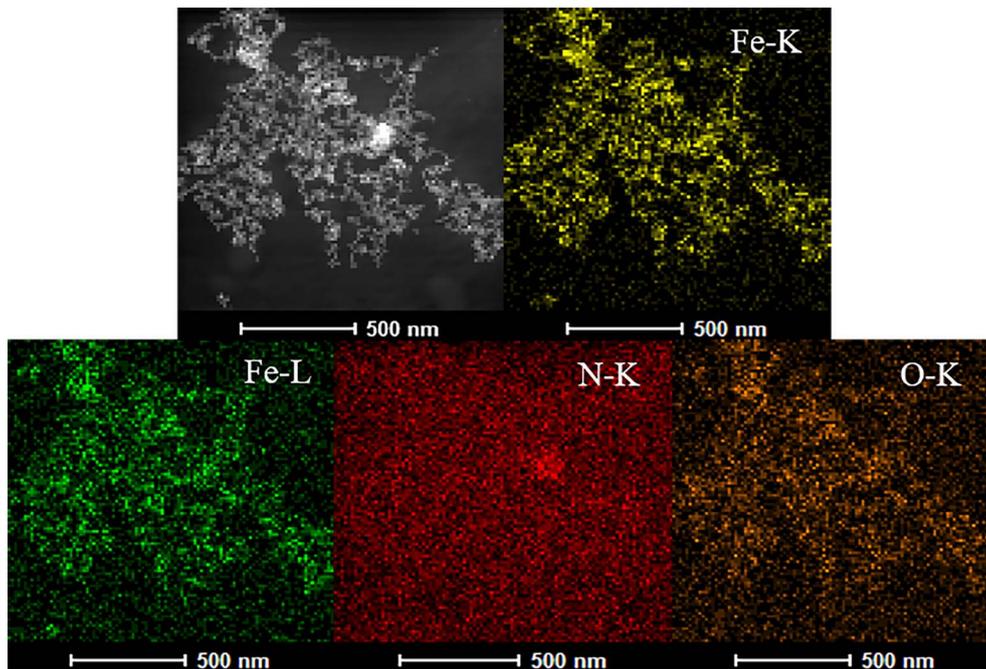
Fig. 3 The elemental mapping of Fe, N and O.

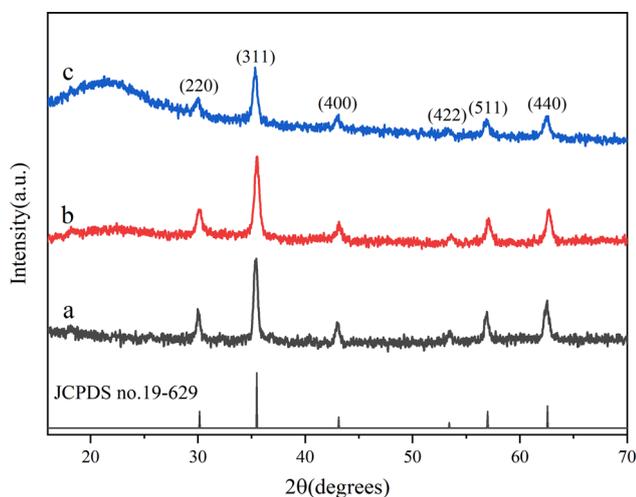Fig. 4 XRD patterns of (a) Fe_3O_4–NH_2, (b) Fe_3O_4–COOH and (c) Fe_3O_4/RhB@PAM.

the C–O–C symmetric and asymmetric stretching vibration, respectively.[45] All of these indicate that Fe_3O_4–COOH was successfully prepared through amide condensation reaction. The infrared absorption peaks of Fe_3O_4/RhB@PAM are shown in Fig. S2c;† the strong absorption peak at 3440 cm^{-1} corresponds to the stretching vibration of –NH_2 in PAM. Also, the signal at 1655 cm^{-1} is the stretching vibration absorption peak of C=O in PAM. The peaks at 1758 cm^{-1} and 1336 cm^{-1} are attributed to the C=O and the C–O stretching vibration of the ester in RhB. Moreover, the peaks at 1591 cm^{-1}, 1467 cm^{-1} and 1414 cm^{-1} correspond to the skeletal vibration of the benzene ring, which further confirms the existence of RhB.

Thermogravimetric (TG) analysis was used to further confirm the existence of the cladding layer, and the results are shown in Fig. 6. One can see that the weight loss within the temperature range of 50–100 °C is due to the physically adsorbed water on the surface of the samples. In Fig. 6a, as the temperature increases, the weight loss rate gradually increases; there is about 4.99% weight loss for Fe_3O_4–NH_2 up to 700 °C, mainly due to the decomposition of 1,6-hexanediamine. In comparison, the weight loss of Fe_3O_4–COOH is about 6.14% (Fig. 6b); the increased amount (1.15%) could be attributed to the decomposition of grafted PEG glycol dicarboxylic acid. While probably due to the decomposition of RhB and PAM, the curve of Fe_3O_4/RhB@PAM nanosensors shows a weight loss of 14.67% (Fig. 6c). These results show that RhB and PAM have wrapped onto the surface of Fe_3O_4–COOH successfully, and the Fe_3O_4/RhB@PAM nanosensors can maintain their structural and functional integrity at a temperature below 100 °C, which is very important for their application in the environment.

The magnetic hysteresis loops of Fe_3O_4–NH_2, Fe_3O_4–COOH and Fe_3O_4/RhB@PAM at room temperature are shown in Fig. 7. As we can see, the saturation magnetization (M_s) of Fe_3O_4–NH_2 (78.86 emu g^{-1}) decreases successively along with the modification of PEG; this is because the PEG is non-magnetic. Similarly, since PAM and RhB are also non-magnetic, the M_s of Fe_3O_4/RhB@PAM (47.59 emu g^{-1}) is much smaller than that of Fe_3O_4–COOH. However, Fe_3O_4/RhB@PAM does not have an obvious pronounced hysteresis loop, indicating that it is superparamagnetic at room temperature. This was also well-verified during the experiment (as shown in the illustration), which would facilitate the rapid separation of Fe_3O_4/RhB@PAM nanosensors from the measured water samples, thereby avoiding secondary pollution.
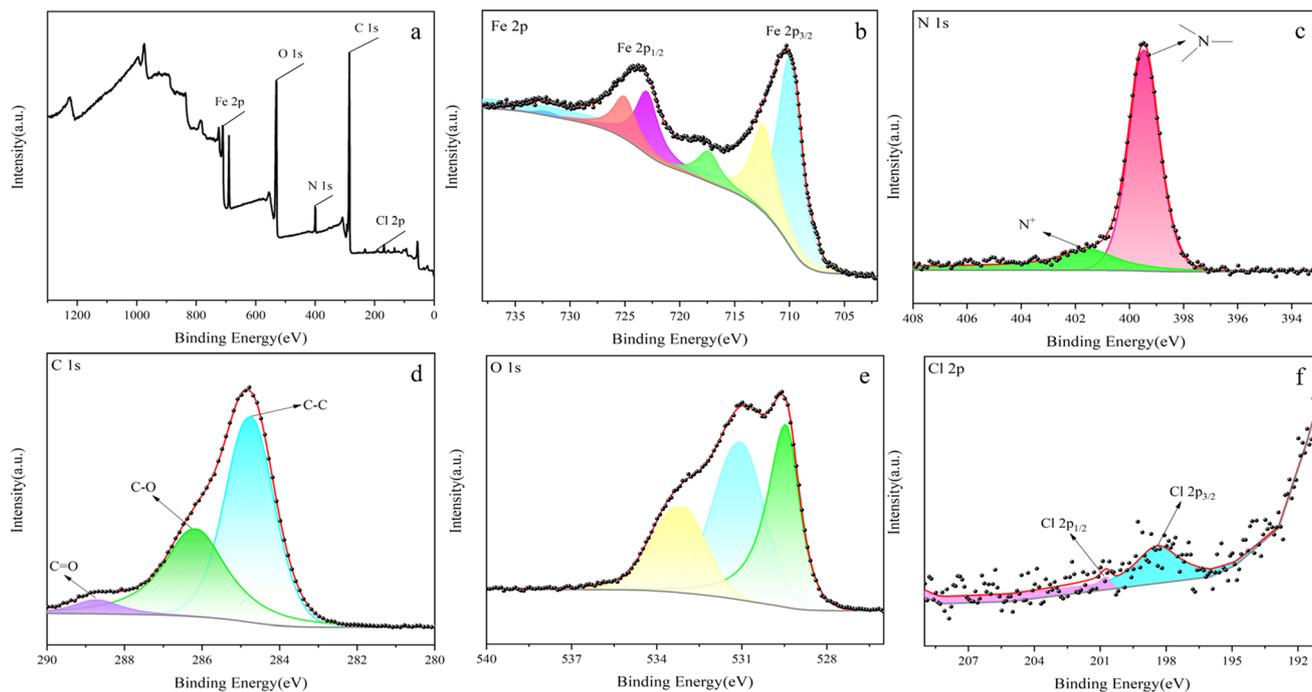
Fig. 5 XPS spectra of (a) Fe_3O_4/RhB@PAM, (b) Fe 2p, (c) N 1s, (d) C 1s, (e) O 1s and (f) Cl 2p of Fe_3O_4/RhB@PAM.
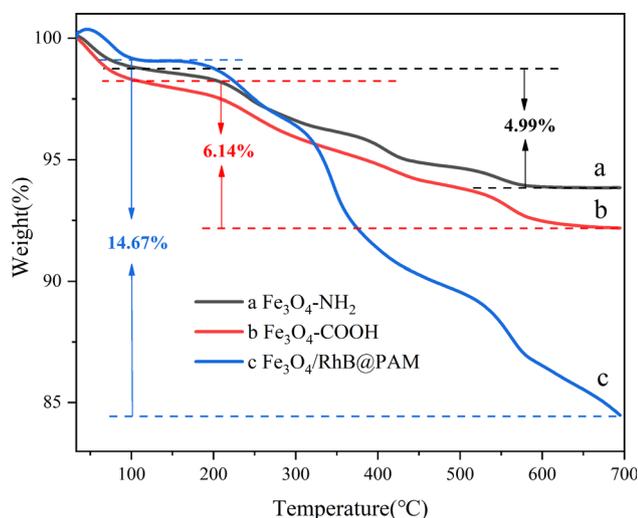
Fig. 6 TG analysis results of (a) $Fe_3O_4–NH_2$, (b) $Fe_3O_4–COOH$ and (c) Fe_3O_4/RhB@PAM.
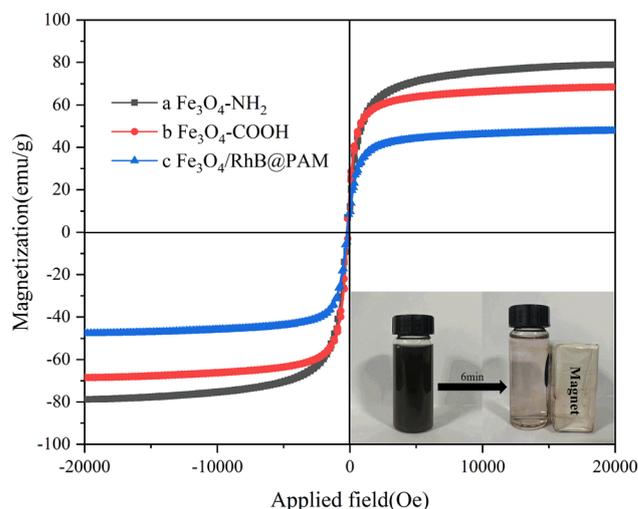
Fig. 7 VSM measurement results of (a) $Fe_3O_4–NH_2$, (b) $Fe_3O_4–COOH$ and (c) Fe_3O_4/RhB@PAM. The illustration is the suspended aqueous solution of Fe_3O_4/RhB@PAM before and after a magnet is placed outside the sample vial for 6 min.

The stability of the Fe_3O_4/RhB@PAM sensor is a problem worthy of our attention. The experiments on the stability of the sensor under various environmental conditions, such as pH, temperature, and long-term storage were carried out. As shown in Fig. S3a,† under acidic conditions (pH < 7), the fluorescence intensity first increases and then decreases with the increase in the pH value. However, there is almost no change in the fluorescence intensity of Fe_3O_4/RhB@PAM in an alkaline environment. This shows that the sensor is relatively stable in an alkaline environment, and the change in the fluorescence intensity in an acidic environment confirms that Fe_3O_4/

RhB@PAM is a pH-sensitive smart sensor. In addition, as the temperature increases, the fluorescence intensity of the sensor does not change significantly, especially below 30 °C, indicating that the sensor has good stability at room temperature (Fig. S3b†). Moreover, it can be seen from Fig. S3c† that the fluorescence intensity of Fe_3O_4/RhB@PAM does not change significantly with the extension of the storage time. All the results indicate that the prepared Fe_3O_4/RhB@PAM has good pH sensitivity and stability.
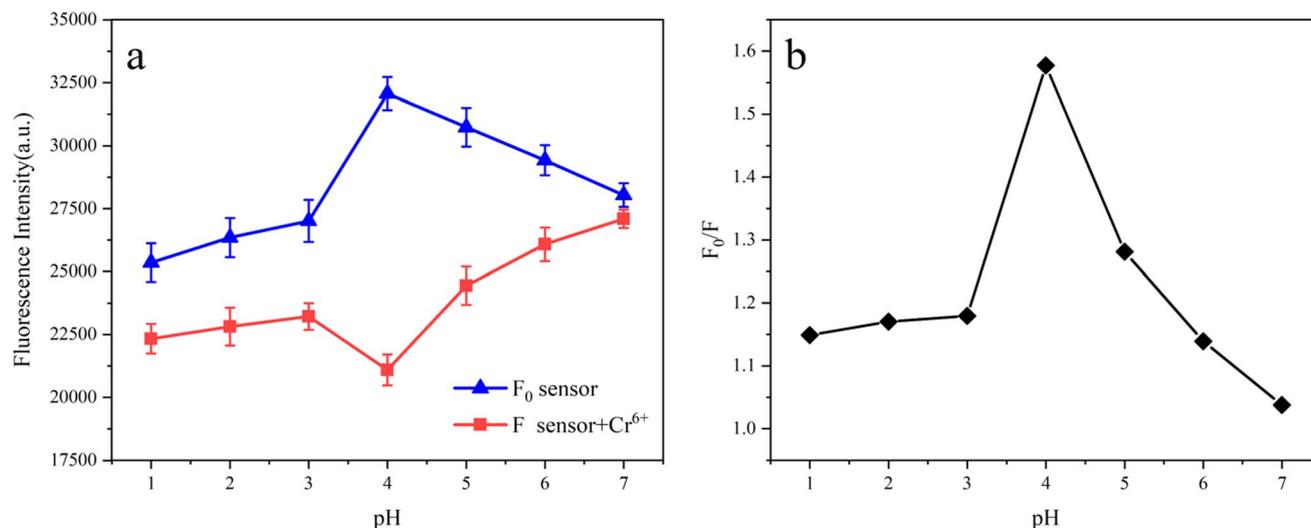
Fig. 8 (a) The plot of the fluorescence intensity of the sensor (F_0) and sensor + Cr(VI) (F) *versus* various pH values, (b) the relationship between the value of F_0/F and pH. The excitation and emission wavelengths were 554 nm and 582 nm, respectively. Slit: 2.0 nm/2.0 nm.

3.2. Effect of pH on Cr(VI) sensing

In order to preferably study the practical applicability of Fe_3O_4/RhB@PAM sensors, the pH response experiments were performed in blank aqueous solution and aqueous solution containing Cr(VI) with different pH. As shown in Fig. 8a, the fluorescence intensity of the Fe_3O_4/RhB@PAM sensor (F_0) increases with the increase in the pH value and reaches its maximum at pH = 4, then the F_0 decreases with the increase in pH. When the Fe_3O_4/RhB@PAM sensor captures Cr(VI), the fluorescence intensity (F) is significantly lower than F_0, and the change pattern of F is completely different from that of F_0, indicating that Fe_3O_4/RhB@PAM is an "ON–OFF" intelligent sensor. Furthermore, the relationship between the value of F_0/F and pH (Fig. 8b) indicated that the optimal working pH of the sensor was 4, and we further studied the capture performance in Cr(VI) solution with pH = 4.

3.3. Selectivity

The effects of competing ions on the capture of Cr(VI) were investigated by recording the fluorescence intensities of environmentally relevant ions, including Cr(VI), Fe^{3+}, Cr^{3+}, Cd^{2+}, Pb^{2+}, Zn^{2+}, Sn^{2+}, Ca^{2+}, NH_4^+, Na^+ and K^+, each with a concentration of 0.75 ppm. The results are presented in Fig. 9. As we expected, the Fe_3O_4/RhB@PAM sensor exhibits high selectivity and low fluorescence intensity only with Cr(VI). Other ions have little influence on the quenching effect of the fluorescence intensity. Moreover, when Cr(VI) was added to the suspension containing competitive ion and Fe_3O_4/RhB@PAM sensors under the same conditions, a significant decrease in the fluorescence intensity was observed (Fig. 10). All of these indicated that the coexistence of various competing ions would not influence the selectivity of Fe_3O_4/RhB@PAM. Unlike any other detection of Cr(VI), which relies on the addition of masking agents and/or requires pretreatment to improve the selectivity, the sensors in this work do not require these.
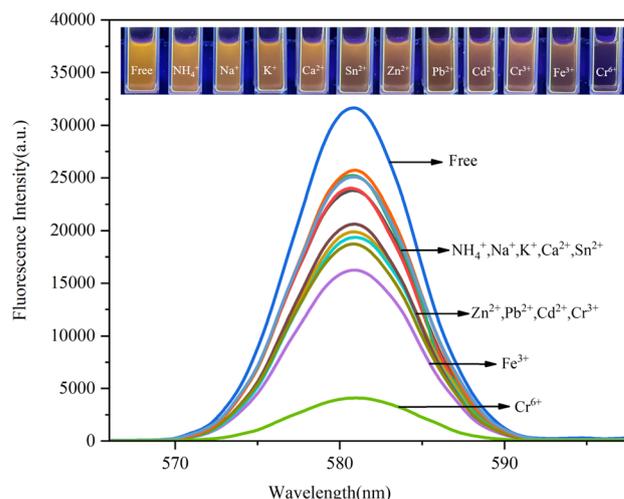

Fig. 9 Fluorescence spectra of Fe_3O_4/RhB@PAM suspensions after the addition of different cations ([cations]/[Fe_3O_4/RhB@PAM] = 1/1.6). The excitation and emission wavelengths were 554 nm and 582 nm, respectively. Slit: 2.0 nm/2.0 nm. Inset: the photographs of the fluorescence changes of Fe_3O_4/RhB@PAM suspensions upon the addition of different cations.

In acidic environments, Cr(VI) can be converted into Cr(III). Therefore, exploring the impact of Cr(III) on the sensor performance is crucial to further study the detection sensitivity for Cr(VI). As shown in Fig. S4a,† with the increase in concentration, the fluorescence intensity of Fe_3O_4/RhB@PAM does not change significantly, confirming that the sensor is insensitive to Cr(III). Moreover, the fluorescence intensities of the Fe_3O_4/RhB@PAM sensor with Cr(III) also do not change significantly at different pH values and concentrations (Fig. S4b and S4c†). Once an equal amount of Cr(VI) was added, the fluorescence intensity of the sensors decreased significantly, especially as the concentration increased; the intensity decreased to a greater extent. All
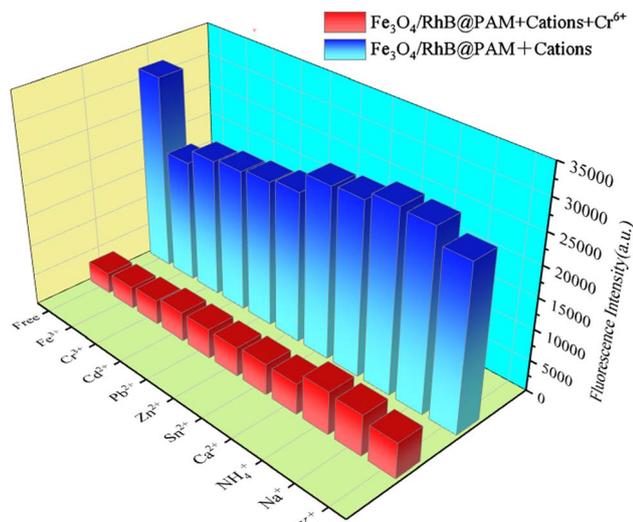
Paper

Fig. 10 Selectivity of Fe_3O_4/RhB@PAM for the capture of Cr(VI) in an aqueous solution (pH 4). The excitation and emission wavelengths were 554 nm and 582 nm, respectively. Slit: 2.0 nm/2.0 nm.

Fig. 11 (a) Fluorescence spectra of Fe_3O_4/RhB@PAM after the addition of different amounts of Cr(VI) in an aqueous solution (pH 4), inset: the photographs of the fluorescence changes of the Fe_3O_4/RhB@PAM suspensions upon the addition of different concentrations of Cr(VI). (b) Plot of the fluorescence intensity *versus* various concentrations of Cr(VI). F_0 is the fluorescence intensity of Fe_3O_4/RhB@PAM sensors; F is the obtained fluorescence intensity after the addition of Cr(VI). The excitation and emission wavelengths were 554 nm and 582 nm, respectively. Slit: 2.0 nm/2.0 nm.

these indicate that the presence of Cr(III) does not affect the selectivity of Fe_3O_4/RhB@PAM towards Cr(VI), whether in Cr(III) alone or Cr(III) and Cr(VI) co-existing solutions.

3.4. Sensitivity

Next, the sensitivity of Fe_3O_4/RhB@PAM to capture Cr(VI) in acidic aqueous solution had been investigated. Firstly, the acidic solutions (pH 4) containing various concentrations of Cr(VI) (0.01 to 1.00 ppm) were prepared. Then, the same amount of Fe_3O_4/RhB@PAM sensors were added into the Cr(VI) solutions to ensure that the concentrations of Fe_3O_4/RhB@PAM were both 1.20 ppm. The resulting solutions were placed in an oscillator at room temperature for 5 min, and then the fluorescence intensity of each solution was measured. As shown in Fig. 11a, with the increase in Cr(VI) concentration, the fluorescence intensity gradually decreased. In addition, by fitting F_0/F and Cr(VI) concentration, it was found that the two have a good linear relationship ($R^2 = 0.9925$, Fig. 11b). Therefore, the limit of detection (LOD) of Fe_3O_4/RhB@PAM sensors (0.347 μM) was successfully derived based on the formula LOD = $K \times$ (SD/S),[46] where K was 2 or 3 (here, we took 2), SD (0.07382) was the standard deviation of the blank solution (pH 4), and S was the slope of the calibration curve (Fig. 11b). However, when RhB alone sensed Cr(VI) under the same conditions, the fluorescence intensity of RhB decreased as the concentration of the metal ion increased (Fig. S5a†). By fitting the concentrations of F_0/F and Cr(VI), it was found that the two had a good linear relationship ($R^2 = 0.9941$, Fig. S5b†). The LOD of RhB was calculated to be 0.436 μM by the formula, which was higher than the value of the Fe_3O_4/RhB@PAM. Through comparison, it was also found that the LOD of the Fe_3O_4/RhB@PAM sensor was particularly attractive because the value was lower than that in some other reports (Table 1) and was also much lower than the value (0.96 μM) permitted by the World Health Organization.[51]
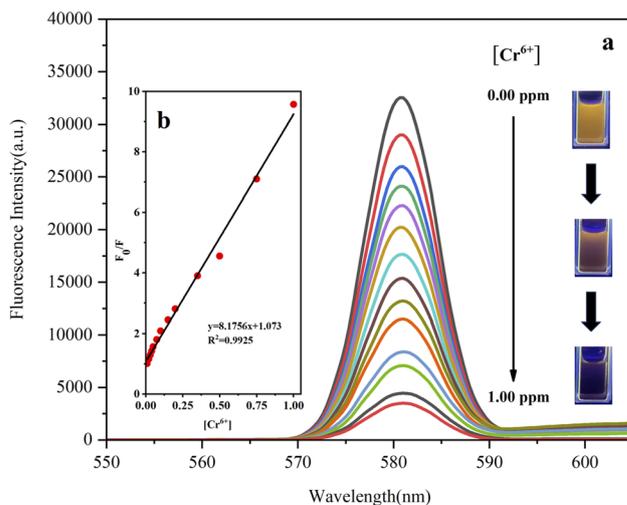
3.5. Proposed sensing mechanism

In addition, the possible mechanism is also proposed. As shown in Fig. 12, in acidic solution (pH 4–7), with the increase in acidity, the hydrolysis of PAM in Fe_3O_4/RhB@PAM was enhanced (inset I), causing the embedded RhB to be released from Fe_3O_4/RhB@PAM, and the fluorescence intensity increased. However, since COOH is a strong electron-withdrawing group, thus, as the pH value further decreased to 1, the ionization degree of COOH decreased, weakening the fluorescence intensity of RhB (inset II). When the Fe_3O_4/RhB@PAM sensor was placed in acidic Cr(VI) solution, the fluorescence intensity of the released RhB was weakened by the complexation with Cr(VI) (inset III). Significantly, at pH = 4, $Cr_2O_7^{2-}$ was reduced by Fe^{2+} in Fe_3O_4 and hydrolyzed ($6Fe^{2+} + Cr_2O_7^{2-} + 14H^+ \rightarrow 6Fe^{3+} + 2Cr^{3+} + 7H_2O$, $Cr_2O_7^{2-} + H_2O \rightarrow 2CrO_4^{2-} + 2H^+$),[52,53] and the RhB released by PAM hydrolysis complexes with CrO_4^{2-} to form a ternary complex, resulting in a sharp decrease in the fluorescence intensity. The extranuclear electron arrangement of Cr(III) is $[Ar]3d^3$, which makes it easy to form a complex with a coordination number of 6. Moreover, RhB has a high steric hindrance and it is difficult to form a 6-coordinated complex with Cr(III). Therefore, the presence of Cr(III) did not affect the selectivity of the Fe_3O_4/RhB@PAM to Cr(VI). However, during pH 5–7, $Cr_2O_7^{2-}$ can hydrolyze itself into CrO_4^{2-} ($Cr_2O_7^{2-} + H_2O \rightarrow 2CrO_4^{2-} + 2H^+$), and CrO_4^{2-} can react with Fe^{2+} to form $Cr(OH)_3$ ($3Fe^{2+} + CrO_4^{2-} + 4H_2O \rightarrow 3Fe^{3+} + Cr(OH)_3 + 5OH^-$), resulting in fluorescence enhancement (primary); meanwhile, the resulting precipitate caused a part of the release pores to be blocked, which caused the partial loss of fluorescence (secondary). As a whole, the fluorescence intensity

Table 1 Comparison of different Cr(VI) sensors

Sensor	Linear range (µM)	LOD (µM)	Ref.
MANCDs	1–150	0.53	47
Gox–chitosan immobilized paper biosensor	0.96–19	0.96	48
ZnO-QCD-hydrogel	0–4.9	1.20	49
N,S CDs	1–40	0.52	50
Fe_3O_4/RhB@PAM	0–20	0.35	This work

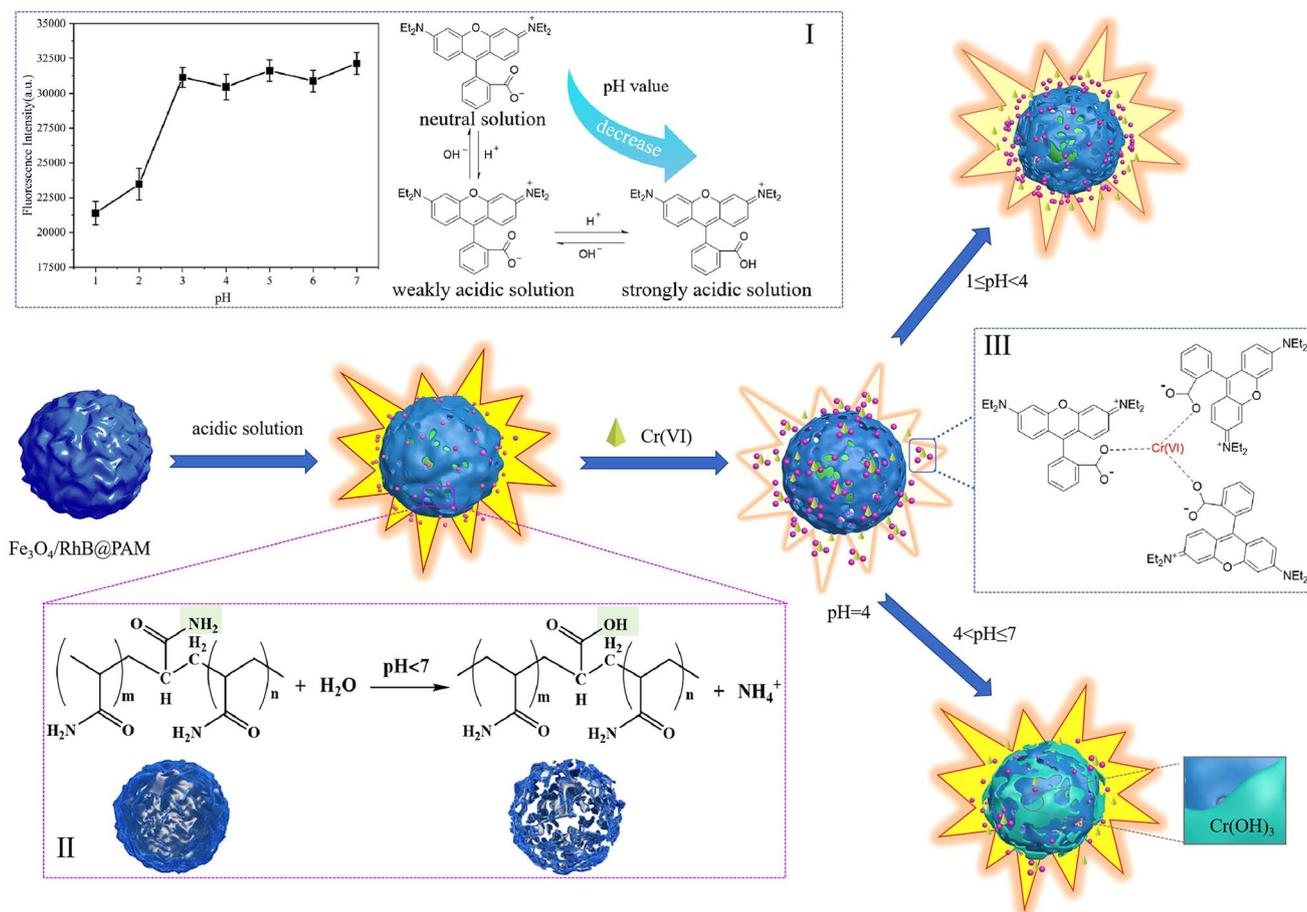**Fig. 12** Schematic diagram of the pH-sensitive controlled capture mechanism of Fe_3O_4/RhB@PAM sensors towards Cr(VI) under acidic conditions. Insets: (I) effect of the pH value of the solution on RhB fluorescence performance and the existing forms of RhB under different acidic conditions, (II) hydrolysis mechanism of PAM under acidic conditions, and (III) the complexation between RhB and Cr(VI).

slightly increased. When the pH value was lower than 4, the COOH of RhB did not ionize and played a dominant role in affecting the fluorescence intensity.

4. Conclusion

In summary, the intelligent magnetic sensor (Fe_3O_4/RhB@PAM) for pH-sensitive controlled capture of Cr(VI) has been successfully prepared *via* a very facile and inexpensive route. On the basis of the reasonable design, the Fe_3O_4 particles endowed Fe_3O_4/RhB@PAM with excellent magnetic properties, enabling rapid separation from the solution and avoiding secondary pollution. The PAM effectively wrapped RhB and Fe_3O_4 particles so as to endow the sensors with good hydrophilicity and pH sensitivity. When the Fe_3O_4/RhB@PAM captured Cr(VI) in acidic environments, especially pH = 4, PAM hydrolyzed to release RhB and complexed with Cr(VI), hindering the ionization of COOH and leading to a decrease in the fluorescence intensity of RhB. Furthermore, the obtained sensors had extraordinary selectivity for Cr(VI) over competitive ions (Fe^{3+}, Cr^{3+}, Cd^{2+}, Pb^{2+},

Zn^{2+}, Sn^{2+}, Ca^{2+}, NH_4^+, Na^+ and K^+), and the limit of detection (LOD) for Cr(vi) in aqueous solutions was lower (0.347 μM) than the value prescribed by the World Health Organization (0.96 μM). Therefore, we have enough reasons to believe that the Fe_3O_4/RhB@PAM sensor is a promising device to be used in acidic solutions for Cr(vi) detection, and this also provides a valuable idea for the effective development of pH-sensitive, environment-friendly, highly selective and sensitive Cr(vi) sensors.

Conflicts of interest

There are no conflicts of interest to declare.

Acknowledgements

References

1 S. Sarfraz, S. Ameer, M. Javed, S. Iqbal, S. O. Aljazzar, M. Zahra, S. Amin, K. H. Shah, M. A. Abourehab, E. B. Elkaeed and N. S. Awwad, *RSC Adv.*, 2022, **12**(37), 23898–23911.

2 T. Cheang, H. Zhou, W. Lin, Y. Wang, X. Chang, F. Gao and Y. Zhang, *J. Mater. Sci.*, 2022, **57**(42), 19694–19703.

3 Y. Su, M. Cui, J. Zhu, Y. Wu, Y. Wei and S. Bian, *J. Mater. Sci.*, 2018, **53**(6), 4078–4088.

4 A. Swaidan, P. Borthakur, P. K. Boruah, M. R. Das, A. Barras, S. Hamieh, J. Toufaily, S. Hamieh, S. Szunerits and R. Boukherroub, *Sens. Actuators, B*, 2019, **294**, 253–262.

5 D. Tai, C. Liu and J. Liu, *Spectrosc. Lett.*, 2019, **52**(3–4), 194–199.

6 X. Zhang, W. Zou and J. Chen, *J. Mater. Sci.*, 2023, **58**(39), 15396–15410.

7 D. Fang, T. Xu, L. Fang, H. Chen, Y. Huang, H. Zhang, Z. Miao, C. Mao, B. Chi and H. Xu, *Sens. Actuators, B*, 2021, **329**, 129219.

8 S. Upadhyay, A. K. Saha and A. Sinha, *J. Environ. Manage.*, 2019, **236**, 388–395.

9 G. Zelmanov and R. Semiat, *Sep. Purif. Technol.*, 2011, **80**(2), 330–337.

10 F. Edition, *WHO Chron.*, 2011, **38**(4), 104–108.

11 C. Wu, O. M. K. Khaing and X. Fan, *ACS Nano*, 2010, **4**(10), 5897–5904.

12 X. Xu, S. Yang, Y. Wang and K. Qian, *Green Analytical Chemistry*, 2022, **2**, 100020.

13 M. Zhang, L. Zhang, H. Tian and A. Lu, *Carbohydr. Polym.*, 2020, **236**, 116037.

14 S. Maharjan, Y. J. Yun, V. A. Okello, G. P. Wiederrecht, D. J. Gosztola and A. J. Ayitou, *J. Photochem. Photobiol., A*, 2022, **424**, 113648.

15 M. Ashafaq, M. Khalid, M. Raizada, M. S. Ahmad, M. S. Khan, M. Shahid and M. Ahmad, *J. Inorg. Organomet. Polym.*, 2020, **30**, 4496–4509.

16 P. Pathak, J. H. Hwang, R. H. T. Li, K. L. Rodriguez, M. M. Rex, W. H. Lee and H. J. Cho, *Sens. Actuators, B*, 2021, **344**, 130263.

17 Y. Chen, Y. Lian, M. Huang, W. Lin and L. Xiao, *Analyst*, 2019, **144**(14), 4250–4257.

18 L. Eskandari, F. Andalib, A. Fakhri, M. K. Jabarabadi, B. Pham and V. K. Gupta, *Int. J. Biol. Macromol.*, 2020, **164**, 4138–4145.

19 H. Zhao, H. Ding, H. Kang, C. Fan, G. Liu and S. Pu, *RSC Adv.*, 2019, **9**(72), 42155–42162.

20 D. Sahu, N. Sarkar, P. Mohapatra and S. K. Swain, *Microchem. J.*, 2020, **154**, 104577.

21 S. E. Hooshmand, B. Baeiszadeh, M. Mohammadnejad, R. Ghasemi, F. Darvishi, A. Khatibi, M. Shiri and F. H. S. Hussain, *Sci. Rep.*, 2023, **13**(1), 17038.

22 I. Y. Denisyuk, A. A. Rybikov and Y. A. Ignat'eva, *Opt. Spectrosc.*, 2021, **129**(4), 471–475.

23 D. Pilnaj, P. Kuráň, M. Šťastný, V. Pilařová, P. Janoš, M. Kormunda and J. Tokarský, *Environ. Technol. Innovation*, 2021, **24**, 101905.

24 M. Kempasiddaiah, V. Kandathil, R. B. Dateer, M. Baidya, S. A. Patil and S. A. Patil, *J. Environ. Sci.*, 2021, **101**, 189–204.

25 M. Oguz, A. A. Bhatti and M. Yilmaz, *Mater. Lett.*, 2020, **267**, 127548.

26 P. M. Singh, A. Tiwari, D. Maity and S. Saha, *J. Mater. Sci.*, 2022, **57**(24), 10836–10862.

27 A. Moges, T. T. I. Nkambule and J. Fito, *J. Environ. Manage.*, 2022, **305**, 114369.

28 C. Chen, H. Yuan, X. Wang, Y. Lin, Y. He and F. Wang, *Chem. Eng. J.*, 2022, **437**, 135365.

29 Y. Chi, Q. Yuan, Y. Li, J. Tu, L. Zhao, N. Li and X. Li, *J. Colloid Interface Sci.*, 2012, **383**(1), 96–102.

30 R. Xie, Y. Qu, M. Tang, J. Zhao, S. Chua, T. Li, F. Zhang, A. E. H. Wheatley and F. Chai, *Food Chem.*, 2021, **364**, 130366.

31 Y. Cai, B. Ren, C. Peng, C. Zhang and X. Wei, *Molecules*, 2021, **26**(11), 3180.

32 W. Wang, R. Ma, Q. Wu, C. Wang and Z. Wang, *J. Chromatogr. A*, 2013, **1293**, 20–27.

33 M. H. Mashhadizadeh and Z. Karami, *J. Hazard. Mater.*, 2011, **190**(1–3), 1023–1029.

34 S. Raha and M. Ahmaruzzaman, *Chem. Eng. J.*, 2020, **395**, 124969.

35 N. Safari, K. Ghanemi and F. Buazar, *J. Environ. Manage.*, 2020, **276**, 111263.

36 F. Liu, Y. Su, C. Ma, P. Xie, J. Zhao and H. Zhang, *Bull. Environ. Contam. Toxicol.*, 2022, **108**, 315–323.

37 S. Liu, Z. Zhou, S. Zhou, J. Cui, Q. Wang, Y. Zhang, J. Lang and Y. Yan, *J. Taiwan Inst. Chem. Eng.*, 2019, **95**, 300–307.

38 H. Guo, H. Sun, Z. Su, S. Hu and X. Wang, *J. Wuhan Univ. Technol.*, 2018, **33**(3), 559–565.

39 H. Zhang, K. Wan, J. Yan, Q. Li, Y. Guo, L. Huang, S. R. B. Arulmani and J. Luo, *J. Environ. Sci.*, 2024, **135**, 118–129.

40 H. Luo, Y. Zhang, Z. Yang, G. Xiong and Y. Wan, *Mater. Chem. Phys.*, 2017, **201**, 130–138.

41 X. Wang, J. Wu, P. Li, L. Wang, J. Zhou, G. Zhang, X. Li, B. Hu and X. Xing, *ACS Appl. Mater. Interfaces*, 2018, **10**(41), 34905–34915.

42 X. Chen, B. Hu, X. Qian, C. Yong, Z. Liu and X. Xing, *J. Biomater. Sci., Polym. Ed.*, 2016, **27**(11), 1187–1199.

43 X. Wang, H. S. Almoallim, Q. Cui, S. A. Alharbi and H. Yang, *Int. J. Biol. Macromol.*, 2021, **171**, 198–207.

44 H. Zhu, J. Wu, M. Fang, L. Tan, C. Chen, N. S. Alharbi, T. Hayate and X. Tan, *RSC Adv.*, 2017, **7**, 36231–36241.

45 C. Han, N. Cai, V. Chan, M. Liu, X. Feng and F. Yu, *Colloids Surf., A*, 2018, **559**, 104–114.

46 J. Li, X. Wang, W. Liu, X. Li, L. Yang, H. Ma, R. Wu and Q. Wei, *Sens. Actuators, B*, 2021, **346**, 130581.

47 S. Ganguly, P. Das, S. Das, U. Ghorai, M. Bose, S. Ghosh, M. Mondal, A. M. Das, S. Banerjee and N. C. Das, *Colloids Surf., A*, 2019, **579**, 123604.

48 A. Dabhade, S. Jayaraman and B. Paramasivan, *3 Biotech*, 2021, **11**, 1–11.

49 A. Truskewycz, S. A. Beker, A. S. Ball, B. Murdoch and I. Cole, *Anal. Chim. Acta*, 2020, **1099**, 126–135.

50 J. Shen, S. Shang, X. Chen, D. Wang and Y. Cai, *Sens. Actuators, B*, 2017, **248**, 92–100.

51 W. H. Organization, *The World Health Report 2005: Make every mother and child count.*, 2005.

52 L. Liu, X. Liu, D. Wang, H. Lin and L. Huang, *J. Cleaner Prod.*, 2020, **257**, 120562.

53 H. Peng, Y. Leng, Q. Cheng, Q. Shang, J. Shu and J. Guo, *Processes*, 2019, **7**(1), 41.